NUMERICAL SIMULATION IN A WAVE TANK FILLED WITH SAND

MAMDOH ALAJMI[1], JOSÉ M. CARCIONE[2,3], AYMAN N. QADROUH[1] and JING BA[3*]

[1] *SAC - KACST, P.O. Box 6086, Riyadh 11442, Saudi Arabia.*
[2] *Istituto Nazionale di Oceanografia e di Geofisica Sperimentale (OGS), Borgo Grotta Gigante 42c, 34010 Sgonico, Trieste, Italy.*
[3] *School of Earth Sciences and Engineering, Hohai University, Nanjing, 211100, P.R. China. jba@hhu.edu.cn*

(Received January 7, 2019; revised version accepted January 30, 2020)

ABSTRACT

Alajmi, M., Carcione, J.M., Qadrouh, A.N. and Ba, J., 2020. Numerical simulation in a wave tank filled with sand. *Journal of Seismic Exploration*, 29: 247-260.

We develop a pseudospectral modeling algorithm for wave propagation in anelastic media with Dirichlet and Neumman boundary conditions. The method also allows to set non-reflecting boundaries. The modeling can be adapted to laboratory experiments, namely the implementation of free-surface, rigid and non-reflecting boundary conditions at the model boundaries, as for instance, a tank to perform physical modeling. The time-domain equations for propagation in a viscoelastic medium are described by the Zener mechanical model, that gives relaxation and creep functions in agreement with experimental results. The algorithm is based on a two-dimensional Chebyshev differential operator for solving the viscoelastic wave equation. The technique allows the implementation of non-periodic boundary conditions at the four boundaries of the numerical mesh, which requires a special treatment of these conditions based on one-dimensional characteristics. In addition, spatial grid adaptation by appropriate one-dimensional coordinate mappings allows a more accurate modeling of complex media, and reduction of the computational cost by controlling the minimum grid spacing. An example is shown, where we compute microseismograms in a tank filled with lossy sand.

KEY WORDS: wave tank, Dirichlet conditions, Neumann conditions, anelasticity, full-wave modeling.

0963-0651/20/$5.00

INTRODUCTION

Wave modeling is a valuable tool for seismic interpretation and an essential part of inversion algorithms. Most problems regarding environmental geophysics, seismic exploration, earthquake seismology and non-destructive testing of materials require the use of full-wave modeling methods based on model discretization (a mesh) (Fagin, 1992; Carcione, 2002, 2014). Boundary conditions play an important role in modeling. In general, absorbing – non-reflecting – boundaries are applied at the sides of the mesh, but there are cases, where specific conditions are required, such as modeling surface and borehole waves (e.g., Carcione, 1992; Farina et al., 2017). These conditions are particular cases of the Dirichlet and Neumann boundaries conditions, for instance a free surface (displacements are zero) and a rigid surface (normal stresses are zero).

An example, where the finite dimensions of the system requires to implement these conditions, are laboratory experiments (physical modeling), such as analog sandbox models. These systems provide cheap data and can be used to study the effects of seismic wave propagation in complex media, and to improve methods of data acquisition, processing and interpretation (Sherlock, 1999; Sherlock and Evans, 2001; Smolkin, 2011; Krawczyk et al., 2013; Bergamo et al., 2014). Numerical modeling is required when physical modeling (laboratory) experiments are performed, in order to interpret the results (Solymosi et al., 2018). In a laboratory experiment, certain boundary condition need to be satisfied, due to the finite dimensions of the physical model. These are basically free-surface, rigid and non-reflecting conditions at the top, bottom and sides of the device, where the experiment is carried out, e.g., a tank (De Angelis, 2010). Hence, we should be able to distinguish between the main event we are interested in and events generated by the finite dimension of the experimental device. In this sense, numerical modeling is essential. For a review and characteristics of small-scale physical modeling, see Solymosi et al. (2018). These authors consider a model immersed in a water tank, and use a conventional pulse-echo technique to collect acoustic reflection data at zero-offset and offset configurations.

We generalize a modeling approach introduced by Carcione (1996) for lossless media to the anelastic case, where wave loss is described by the Zener mechanical model. The fact that attenuation and velocity dispersion are modeled is essential to describe wave propagation in unconsolidated media such as sand, since this type of media is highly anelastic. This realistic description is important to analyze near-surface seismic data. We recast the elastodynamic equations in the particle-velocity/stress formulation. The numerical method is based on the pseudospectral Chebyshev differential operator to compute the spatial derivatives and the 4th-order Runge-Kutta method for time stepping. The 2D physical domain is discretized at a set of points obtained from a 2D Chebyshev grid (computational domain) after application of two 1D stretching transformations to each Cartesian co-ordinate. By stretching the mesh we increase the grid spacing and use time steps of the order $O(N^{-1})$ (Kosloff and Tal-Ezer, 1993; Carcione, 1996).

The Chebyshev pseudospectral method facilitates the implementation of general boundary conditions at the four boundaries of the mesh and is adapted for domain-decomposition problems as well (Carcione et al., 2018). This problem is solved by modifying the wave equation by imposing the correct behaviour on the 1D characteristics normal to the boundaries (Carcione, 1996).

EQUATIONS OF MOTION

The equations of motion in the (x,z)-plane, based on memory variables (e.g., Carcione and Helle, 2004), are given in the following:

The equations of momentum conservation:

$$\dot{v}_x = \frac{1}{\rho}\left(\sigma_{xx,x} + \sigma_{xz,z}\right) + f_x, \tag{1}$$

$$\dot{v}_z = \frac{1}{\rho}\left(\sigma_{xz,x} + \sigma_{zz,z}\right) + f_z, \tag{2}$$

where v_x and v_z are the particle velocities, σ_{xx}, σ_{zz} and σ_{xz} are the stress components, ρ is the density and f_x and f_z are the body forces. A dot above a variable denotes time differentiation, and the subindices "$,x$" and "$,z$" indicate spatial derivatives with respect to the Cartesian coordinates.

The constitutive equations:

$$\dot{\sigma}_{xx} = \lambda\vartheta + 2\mu v_{x,x} + \lambda e_1 + \mu\left(e_1 + e_2\right), \tag{3}$$

$$\dot{\sigma}_{zz} = \lambda\vartheta + 2\mu v_{z,z} + \lambda e_1 + \mu\left(e_1 - e_2\right), \tag{4}$$

$$\dot{\sigma}_{xz} = \mu\left(v_{x,z} + v_{z,x} + e_3\right), \tag{5}$$

where $\vartheta = v_{x,x} + v_{z,z}$ is the dilatation, e_1, e_2 and e_3 are memory variables, and λ and μ are the unrelaxed (high-frequency) Lamé constants, respectively.

The memory-variable equations:

$$\dot{e}_1 = \left(\frac{1}{\tau_\varepsilon^{(1)}} - \frac{1}{\tau_\sigma^{(1)}}\right)\vartheta - \frac{e_1}{\tau_\sigma^{(1)}}, \tag{6}$$

$$\dot{e}_2 = \left(\frac{1}{\tau_\varepsilon^{(2)}} - \frac{1}{\tau_\sigma^{(2)}}\right)\left(v_{x,x} - v_{z,z}\right) - \frac{e_2}{\tau_\sigma^{(2)}}, \tag{7}$$

$$\dot{e}_3 = \left(\frac{1}{\tau_\varepsilon^{(2)}} - \frac{1}{\tau_\sigma^{(2)}} \right) \left(v_{x,z} + v_{z,x} \right) - \frac{e_3}{\tau_\sigma^{(2)}}, \tag{8}$$

where $\tau_\sigma^{(\nu)}$ and $\tau_\varepsilon^{(\nu)}$ are material relaxation times, corresponding to dilatational $(\nu = 1)$ and shear $(\nu = 2)$ deformations. The relaxation times can be expressed as

$$\tau_\varepsilon^{(\nu)} = \frac{\tau_0}{Q_\nu} \left(\sqrt{Q_\nu^2 + 1} + 1 \right), \qquad \tau_\sigma^{(\nu)} = \tau_\varepsilon^{(\nu)} - \frac{2\tau_0}{Q_\nu}, \tag{9}$$

where τ_0 is a relaxation time such that $1/\tau_0$ is the center frequency of the relaxation peak and Q_ν are the minimum quality factors. We assume $\tau_0 \omega_0 = 1$, where ω_0 is a reference frequency that can be the dominant frequency of the source. The quality factor, Q_1, associated with the bulk modulus, is obtained from the relation

$$\frac{1+\alpha}{Q_1} = \frac{3(1-\alpha)}{Q_P} - \frac{2(1-2\alpha)}{Q_2}, \qquad \alpha = \frac{\left(v_P / v_S \right)^2 - 2}{2\left[\left(v_P / v_S \right)^2 - 1 \right]}, \tag{10}$$

where α is Poisson's ratio, and Q_P is the P-wave quality factor, while the S-wave quality factor is $Q_S = Q_2$. Here v_P and v_S are the unrelaxed (infinite-frequency) velocities.

NUMERICAL ALGORITHM

The spatial differential operator is based on the Chebyshev method whose collocation points define the numerical mesh of the computational domain. From this, the physical domain is obtained after mapping transformations which circumvent the severe stability condition of the time integration scheme and yield spatially adaptive grids. The implementation of boundary conditions requires a special treatment based on characteristics variables.

Chebyshev Collocation Method

The computational domain is a square region $(\xi, \eta) \in [1, -1] \times [1, -1]$, where the grid distribution is defined by the Chebyshev Gauss-Lobatto points. Let

us assume that the pair (ζ, N) represents either (ξ, N_x) or (η, N_z), where N_x and N_z are the number of grid points in the *x*- and *z*-directions, respectively. A field variable $u(\zeta)$, $-1 \le \zeta \le 1$, can be expanded into Chebyshev polynomials $T_n(\zeta)$ as

$$u(\zeta_j) = \sum_{n=0}^{N}{}'' a_n T_n(\zeta_j), \tag{11}$$

where $\zeta_j = \cos(\pi j / N)$, $j = 0,\ldots, N$, are the Gauss-Lobatto collocation points, and $\sum''$ halves the first and last terms. The first-order derivative of *u* is given by

$$\frac{\partial u}{\partial \zeta} = \sum_{n=0}^{N}{}'' b_n T_n(\zeta_j), \quad b_{n-1} = b_{n+1} + 2n a_n, \; n = N,\ldots,1, \tag{12}$$

initiating the recursion equation with $b_{N+1} = b_N = 0$. The spatial derivative is computed via a variant of the fast Fourier transform (FFT) for the cosine transform (Carcione, 2014).

Coordinate mapping

The uneven distribution of points of the Chebyshev differential operator has two main disadvantages. In the first place, the stability condition and the accuracy of the time integration scheme depend on the minimum grid spacing of the mesh. The dense concentration of points of the Chebyshev mesh at the boundaries requires time steps of the order $O(N^{-2})$, making the modeling algorithm highly inefficient. This problem is solved by expanding the solution as a finite sum of non-polynomial basis functions. This is achieved by 1D transformations or stretching functions which applied to the Gauss-Lobatto points yield a numerical grid that can be adapted to the particular structure of the model and boundary conditions. The transformations allow time steps of order $O(N^{-1})$, thus reducing considerably the computer time.

We consider the following coordinate transformation from the computational to the physical domain:

$$z_j = z_{\max}\left[\frac{q(\zeta_j) - q(1)}{q(-1) - q(1)}\right], \qquad j = 0,\ldots, N, \tag{13}$$

where

$$q(\xi) = \frac{\arcsin(\gamma\zeta)}{\arcsin(\gamma)}, \tag{14}$$

is a symmetric mapping function satisfying $q(1) = 1$ and $q(-1) = -1.$

The transformation (13) maps the interval $[1,-1]$ onto the interval $[0, a_{\max}]$, where *a* represents *x* or *z,* such that the physical domain is $(x,z) \in [0, x_{\max}] \times [0, z_{\max}]$.

The spatial derivative of a field variable in the physical domain is then given by

$$u_{,z} = u_{,\xi} \cdot \xi_{,z} = \left[\frac{q(-1) - q(1)}{z_{\max}}\right] \xi_{,q} \cdot u_{,\xi}\,. \tag{15}$$

We have

$$\xi_{,q} = \frac{\arcsin(\gamma)}{\gamma} \sqrt{1 - \gamma^2 \xi^2}\,. \tag{16}$$

This mapping stretches the mesh at the boundaries. When $\gamma \to 0$, we obtain the Gauss-Lobatto collocation points, and $\gamma \to 1$ gives equally distributed points as in the Fourier differential operator. The mapping improves the π criterium for resolving the maximum wavenumber to almost two points per minimum wavelength, as in the Fourier case. A detailed analysis of resolution and accuracy of the 1D differential operator constructed with this transformation are given by Kosloff and Tal-Ezer (1993).

Boundary conditions

At each time step of the algorithm, the boundary conditions are implemented. However, a direct application of these conditions gives unstable solutions. This problem is solved by decomposing the wavefield into one-way modes (or characteristics) perpendicular to the boundaries, and modifying these modes according to the boundary conditions (Carcione, 1996, 2014). In the following, the boundary equations for the upper (upper sign) and lower (lower sign) boundaries of the numerical mesh are given.

The Neumann boundary equations are

$$\dot{v}_x^{new} = \dot{v}_x^{old} + \frac{1}{Z_S}\left(\pm \dot{\sigma}_{xz}^{old} - \dot{f} \right), \tag{17}$$

$$\dot{v}_z^{new} = \dot{v}_z^{old} \pm \frac{1}{Z_P}\left(\dot{\sigma}_{zz}^{old} - \dot{g} \right), \tag{18}$$

$$\dot{\sigma}_{xx}^{new} = \dot{\sigma}_{xx}^{old} - \frac{\lambda}{\lambda + 2\mu}\left(\dot{\sigma}_{zz}^{old} - \dot{g} \right), \tag{19}$$

$$\dot{\sigma}_{zz}^{new} = \dot{g}, \tag{20}$$

$$\dot{\sigma}_{xz}^{new} = \pm \dot{f}, \tag{21}$$

where f and g are time-dependent functions, and $Z_P = \sqrt{(\lambda + 2\mu)\rho}$ and $Z_S = \sqrt{\mu\rho}$ are the compressional and shear impedances. The superscripts (old) and (new) refer to the variables before and after modification of the incoming characteristics. When $f = g = 0,$ we have the free-surface boundary conditions. The method can be used also to plug a source function at a given point of the boundary. For instance, $f = 0$, and $\dot{\sigma}_{zz}(x_0, t) = \dot{g}(t)$ is a vertical force located at x_0 with time history $g(t)$.

The Dirichlet boundary equations are

$$\dot{v}_x^{new} = \dot{v}, \tag{22}$$

$$\dot{v}_z^{new} = \pm \dot{w}, \tag{23}$$

$$\dot{\sigma}_{xx}^{new} = \dot{\sigma}_{xx}^{old} + \frac{\lambda}{\lambda + 2\mu}\left(\dot{\sigma}_{zz}^{old} - \dot{\sigma}_{zz}^{old} \right), \tag{24}$$

$$\dot{\sigma}_{zz}^{new} = \dot{\sigma}_{zz}^{old} + Z_P\left(\pm \dot{v}_z^{old} - \dot{w} \right), \tag{25}$$

$$\dot{\sigma}_{xz}^{new} = \dot{\sigma}_{xz}^{old} \pm Z_S\left(\dot{v}_x^{old} - \dot{v} \right), \tag{26}$$

where v and w are time-dependent functions. Rigid boundary conditions imply $w = v = 0$.

The non-reflecting boundary equations are

$$\dot{v}_x^{new} = \frac{1}{2}\left(\dot{v}_x^{old} \pm \frac{1}{Z_S} \dot{\sigma}_{xz}^{old} \right), \tag{27}$$

$$\dot{v}_z^{new} = \frac{1}{2}\left(\dot{v}_z^{old} \pm \frac{1}{Z_P} \dot{\sigma}_{zz}^{old} \right), \tag{28}$$

$$\dot{\sigma}_{xx}^{new} = \dot{\sigma}_{xx}^{old} - \frac{\lambda}{2(\lambda+2\mu)}\left(\dot{\sigma}_{zz}^{old} \mp Z_P \dot{v}_z^{old} \right), \tag{29}$$

$$\dot{\sigma}_{zz}^{new} = \frac{1}{2}\left(\dot{\sigma}_{zz}^{old} \pm Z_P \dot{v}_z^{old} \right), \tag{30}$$

$$\dot{\sigma}_{xz}^{new} = \frac{1}{2}\left(\dot{\sigma}_{xz}^{old} \pm Z_S \dot{v}_x^{old} \right), \tag{31}$$

The equations for the left boundary can be obtained from the lower boundary equations by substituting $x \rightarrow z$ and $z \rightarrow x$. Similarly, the equations for the right boundary are obtained from the left boundary equations by substituting $x \rightarrow -x$, where in this case, $v_x \rightarrow -v_x$ and $\sigma_{xz} \rightarrow -\sigma_{xz}$.

For the corner points, we use an ad hoc treatment introduced by Lie (1991) who defines the normal to the corner point inwards and bisecting the angle between the adjacent boundary lines. For a rectangular mesh this angle is a multiple of $\pi/4$ depending on the corner point (Carcione, 1996).

The numerical solution obtained with this algorithm has been verified by comparison to the analytical solution of Lamb's problem in Carcione (1996), that is, the response of an elastic (lossless) half-space bounded by a free surface to an impulsive vertical force, f_y (there is no analytical solution in the anelastic case). The L2 error of this comparison is less than 0.1% for typical values of the time step and number of grid points. The error can be further reduced at the cost of increasing the computer time.

EXAMPLE

A practical example is given by a tank to perform laboratory acoustics experiments. The characteristics of the tank and medium properties are shown in Fig. 1 (e.g., Al-Shuhail, 2018). The simulations use a numerical mesh with n_x = 121 and n_z = 81 grid points, with maximum grid sizes of $dx = 1.340$ cm and $dz = 1.569$ cm at the center of the mesh. According to the sampling theorem, the grid can support a maximum frequency of $f_{\max}$ = $c_{\min}/(2d_{\max})$. Since, $c_{\min}$ = 260 m/s, and $d_{\max} = dx$, we have $f_{\max} = 8.285$ kHz.

The source is a vertical force and its time history (a Ricker wavelet) is $h(t)=(a-0.5)\exp(-a)$, $a=[\pi f_P(t-t_s)]^2$, $t_S=1.3/f_P$, with $f_P=3$ kHz, the source central frequency. The spectrum of this source is a Gaussian function with center at f_P, which can be considered the dominant frequency ($2f_P$ should not exceed $f_{\max}$). The dominant wavelengths of the P- and S-waves are (450 m/s)/3000 Hz = 15 cm, and (260 m/s)/3000 Hz = 8.6 cm, respectively.

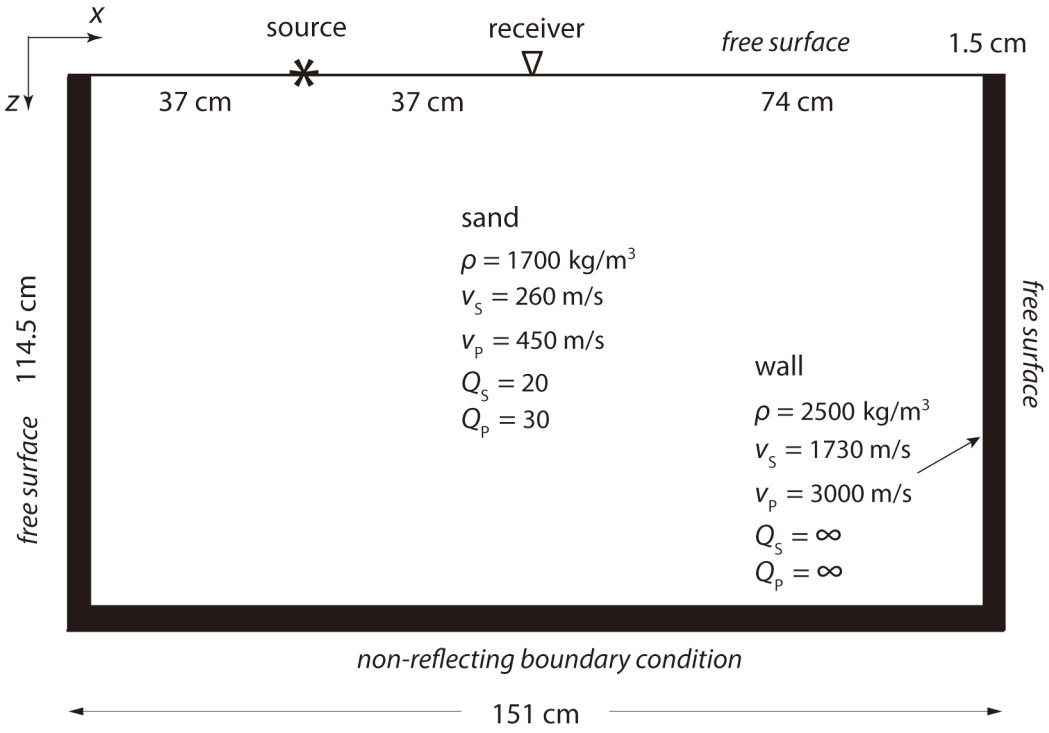

Fig. 1. Model and source-receiver locations. The boundary conditions at the four sides of the mesh are indicated in italics font.

This is an idealized case, since these wavelengths (and frequency) cannot be supported by an unconsolidated medium such as sand. Actually, unconsolidated sand has a low quality factor and the major cause of the severe energy attenuation in dry sand is friction between the grains due to variations in size and roundness. Sample P1 in Prasad and Meissner (1992) (their Fig. 3) is coarse dry sand and has a P-wave quality less than 10 and a S-wave quality factor of approximately 10 at low differential pressures and at a frequency of 100 kHz. On the other hand, Barrière et al. (2012) report a P-wave quality of the order of 5 at low water saturations and 1.6 kHz (their Fig. 6).

The time step of the Runge-Kutta integration scheme is $dt = 5 \times 10^{-7}\,\mathrm{s} = 0.5\,\mu\mathrm{s}$. The first example considers a homogeneous medium, with a source at the surface. Figs. 2 and 3 show the snapshots at 3 ms seismograms of the tank (a) and a half space (b), the latter being computed with non-reflecting boundary conditions at the sides and bottom of the mesh, i.e., with and without the walls. We can see the Rayleigh wave (R), the P-wave and the S-wave, and the reflected events from the left wall.

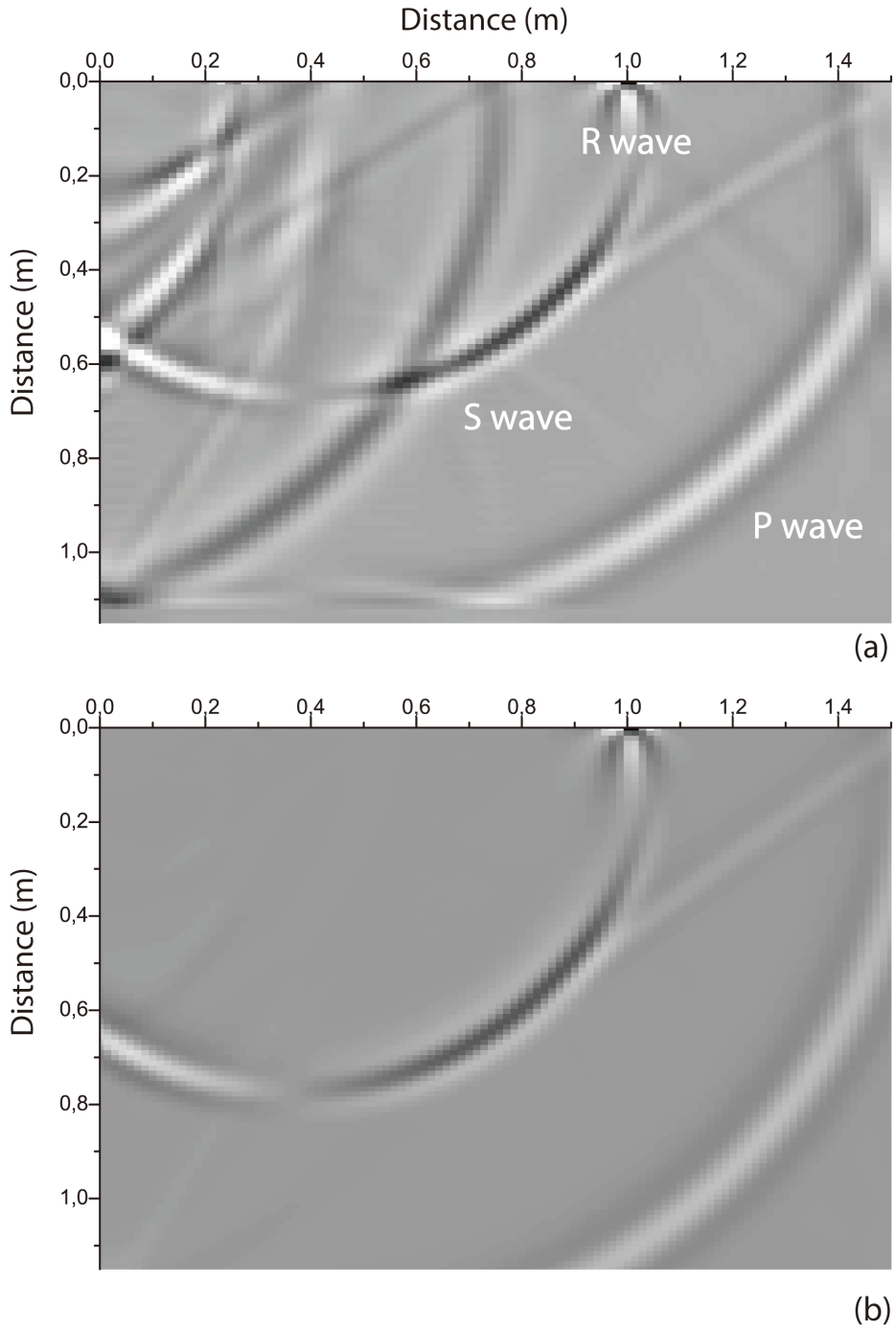

Fig. 2. v_x -snapshots with (a) and without (b) walls. R, P and denote the primary Rayleigh, P- and S-waves. The model corresponds to the tank shown in Fig. 1. The source has a dominant frequency of 3 kHz.

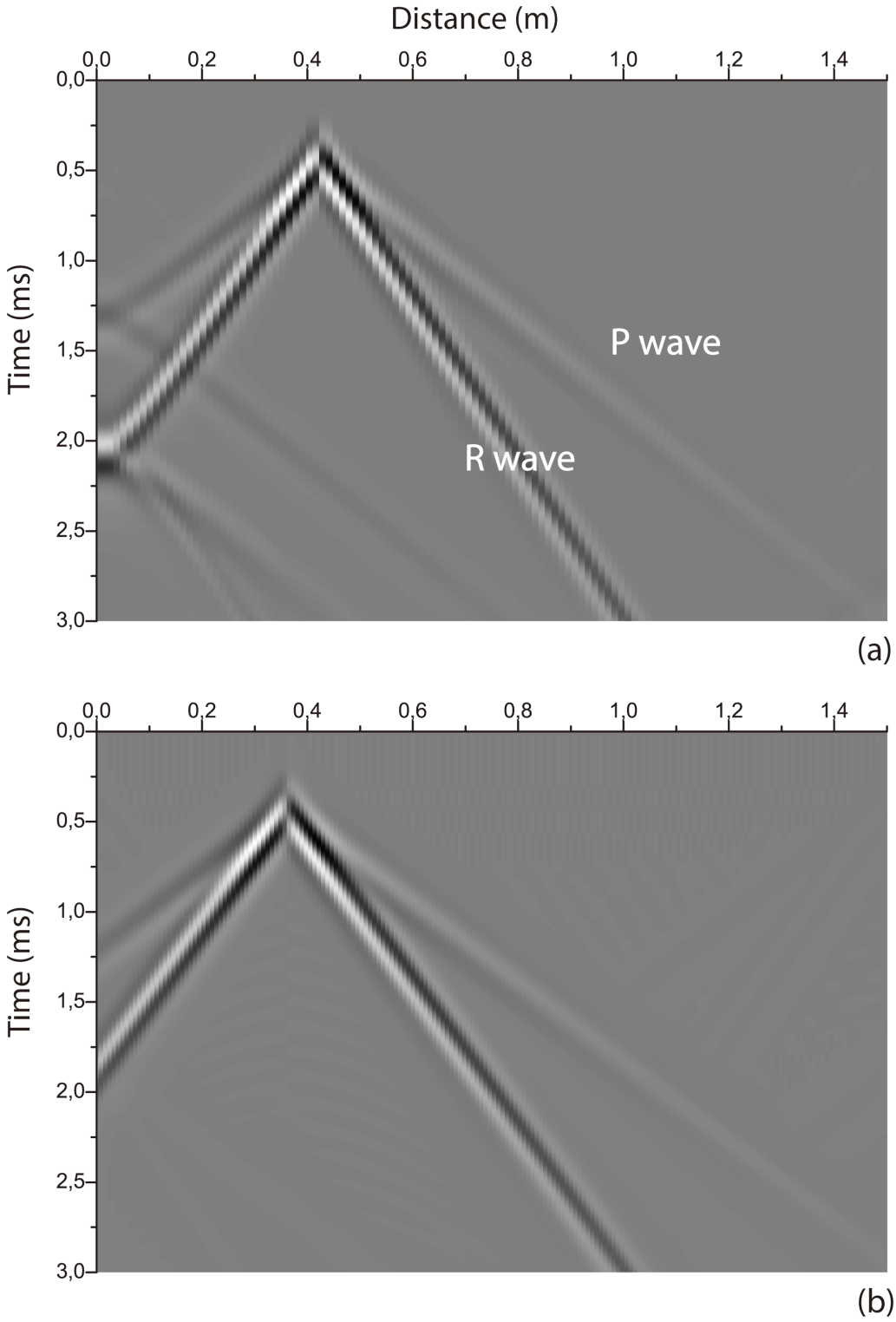

Fig. 3. v_x -seismograms with (a) and without (b) walls. R, P and S denote the Rayleigh, P- and S-waves. The model corresponds to the tank shown in Fig. 1. The source has a dominant frequency of 3 kHz.

Next, we assume a more realistic peak frequency of f_P = 300 Hz, so that dominant wavelengths of the P- and S-waves are (450 m/s)/300 Hz = 1.5 m and (260 m/s)/300 Hz = 0.86 m, respectively. In this case, we consider

$Q_P = 5$ and $Q_S = 10$, i.e., realistic values at seismic frequencies, and smaller than the quality factor assumed at sonic frequencies, since the quality factor depends on frequency and cannot be scaled. The comparison between the anelastic (black line) and elastic (red line) solutions is shown in Fig. 4, indicating attenuation and velocity dispersion of the wavefield. Note the phase discrepancy between 12 and 17 ms. This is due to the strong velocity dispersion caused by anelasticity, since each Fourier component of the wave field travels with a different phase velocity. Fig. 5 shows the effect of the walls on the wavefield, where the reverberations generate the strong coda wave, that disappears in the case of nonreflecting sides.

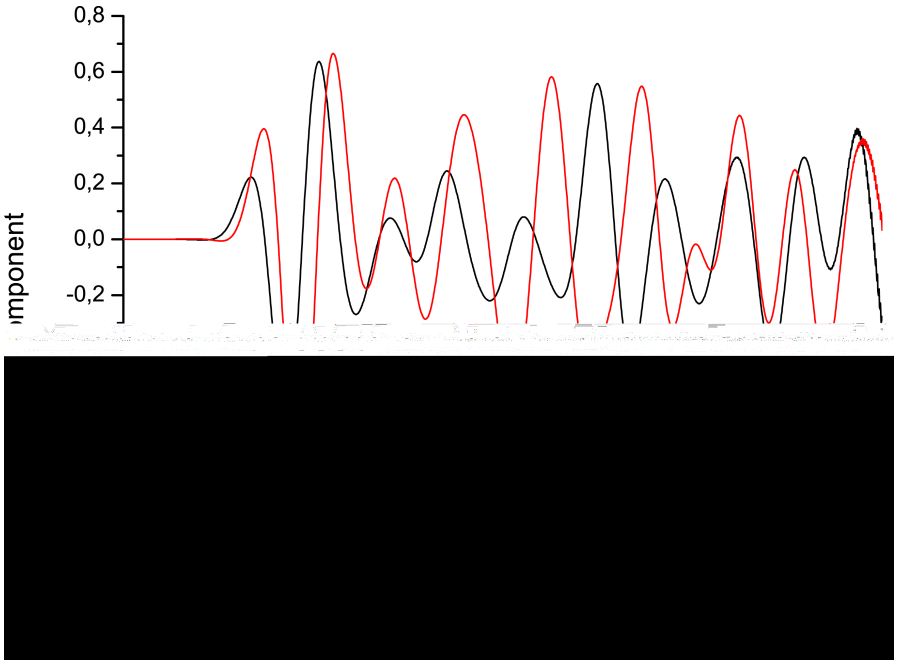

Fig. 4. v_x -seismograms. Comparison between the anelastic (black line) and elastic (lossless) (red line) solutions. The source has a dominant frequency of 300 Hz, $Q_P = 5$ and $Q_S = 10$.

CONCLUSIONS

We have generalized an elastic (lossless) wave modeling algorithm to the anelastic (lossy) case, based on the Zener viscoelastic model. The sides of the mesh can satisfy Dirichlet and Neumann. Examples are zero displacements (or particle velocities) and stress-free conditions, respectively. The method allows the implementation of absorbing-non-reflecting-conditions as well. The wave equation is solved with a 2D Chebyshev pseudospectral operator to compute the spatial derivatives and a time-stepping Runge-Kutta method. We illustrate the method with an example of a tank used to perform laboratory acoustic experiments. The modeling algorithm can be used to simulate acoustic responses to plan real physical experiments.

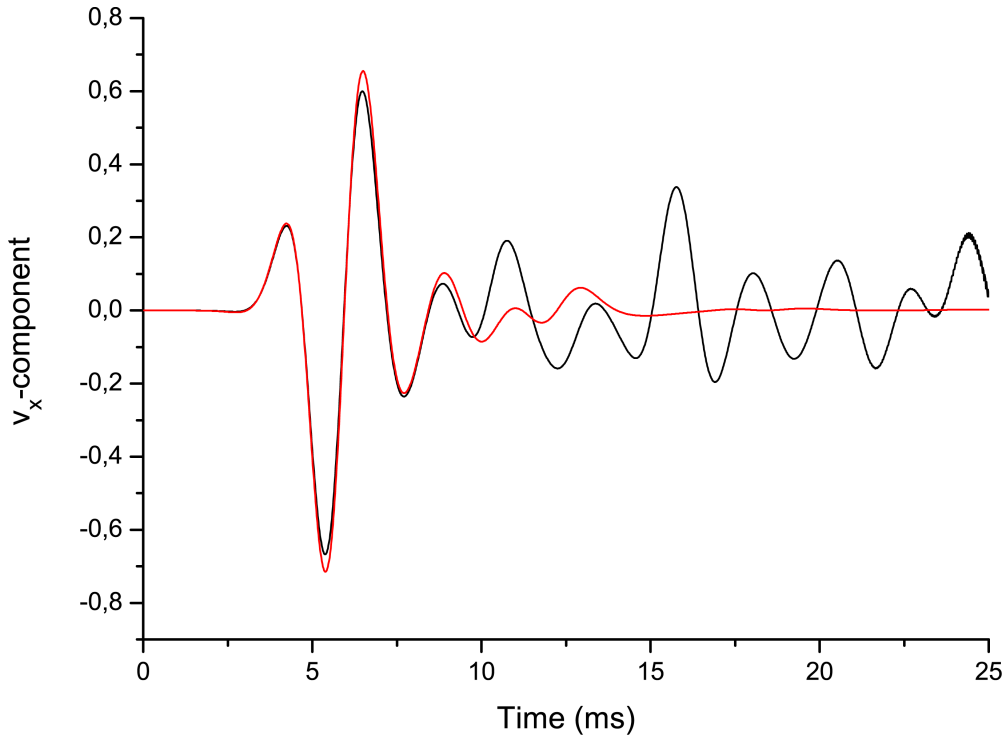

Fig. 5. v_x -seismograms. Comparison between the tank with (black line) and without (red line) reflecting sides (or walls). The source has a dominant frequency of 300 Hz, $Q_P = 5$ and $Q_S = 10$.

ACKNOWLEDGMENTS

The National Natural Science Foundation of China (Grant No. 41974123, 41704109), Jiangsu Innovation and Entrepreneurship Plan, Specially-Appointed Professor Plan of Jiangsu Province, and the Fundamental Research Funds for the Central Universities, China (Grant No. 2016B13114).

REFERENCES

Al-Shuhail, A.A., Alsaleh, M.H. and Sanuade, O.A., 2018. Analysis of time-depth data in sand dunes from the empty quarter desert of Southeastern Saudi Arabia. Arab. J. Sci. Engineer. doi.org/10.1007/s13369-018-3178-2

Barrière, J., Bordes, C., Brito, D., Sénéchal, P. and Perroud, H., 2012. Laboratory monitoring of P waves in partially saturated sand. Geophys. J. Internat., 191: 1152-1170.

Berg, P., If, F., Nielsen, P. and Skovgaard, O., 1994. Analytical reference solutions. In: Helbig, K. (Ed.), Modeling the Earth for Oil Exploration. Pergamon Press, Oxford: 421-427.

Bergamo, P., Bodet, L., Socco, L.V., Mourgues, R. and Tournat, V., 2014. Physical modelling of a surface-wave survey over a laterally varying granular medium with property contrasts and velocity gradients, Geophys. J. Internat., 197: 233-247.

Carcione, J.M., 1996. A 2-D Chebyshev differential operator for the elastic wave equation, Comput. Meth. Appl. Mech. Engineer., 130: 33-45.

Carcione, J.M., Herman, G. and ten Kroode, F.P.E., 2002. Seismic modeling, Geophysics, 67: 1304-1325.

Carcione, J.M., 2014. Wave fields in real media: Wave propagation in anisotropic, anelastic, porous and electromagnetic media. Handbook of Geophysical Exploration, Vol. 38, 3rd revised, extended ed., Elsevier Science Publishers, Amsterdam.

Carcione, J.M., Bagaini, C., Ba, J. Wang, E. and Vesnaver, A., 2018. Waves at fluid-solid interfaces: Explicit versus implicit formulation of the boundary condition. Geophys. J. Internat., 215: 37-48,

De Angelis, M., Giannini, R. and Paolacci, F., 2010. Experimental investigation on the seismic response of a steel liquid storage tank equipped with floating roof by shaking table tests. Earthq. Engineer. Struct. Dyn., 39: 377-396.

Fagin, S.W., 1992. Seismic Modeling of Geological Structures: Applications to Exploration Problems. Geophys. Develop. Series, Vol. 2. SEG, Tulsa, OK.

Farina, B., Poletto, F. and Carcione, J.M., 2017. Synthetic waveforms of axial motion in a borehole with drill string, J. Acoust. Soc. Am., 141: 828-839.

Kosloff, D. and Tal-Ezer, H., 1993. A modified Chebyshev pseudospectral method with an $O\left(N^{-1}\right)$ time step restriction. J. Comput. Phys., 104: 457-469.

Krawczyk, C.M., Buddensiek, M.-L., Oncken, O. and Kukowski, N., 2013. Seismic imaging of sandbox experiments-laboratory hardware setup and first reflection seismic sections, Solid Earth, 4: 93-104.

Lie, I., 1991. Ocean/bottom acoustic interaction with arbitrary bottom profile. FFI/Report-91/7009, NDRE.

Prasad, M. and Meissner, R., 1992. Attenuation mechanisms in sands: Laboratory versus theoretical (Biot) data. Geophysics, 57: 710-719.

Sherlock, D.H., 1999. Seismic Imaging of Sandbox Models. Ph.D. thesis, Curtin University of Technology, Perth.

Sherlock, D.H. and Evans, B.J., 2001. The development of seismic reflection sandbox modelling, AAPG Bull., 85: 1645-1659.

Smolkin, D., 2011. Laboratory scale seismic analysis of a spatially variable hydrological surface in unconfined, unconsolidated sand. M.Sc.thesis, Louisiana State University, Baton Rouge, LA.

Solymosi, B., Favretto-Cristini, N., Monteiller, V., Komatitsch, D., Cristini, P., Arntsen, B. and Ursin, B., 2018. How to adapt numerical simulation of wave propagation and ultrasonic laboratory experiments to be comparable - A case study for a complex topographic model. Geophysics, 83(4): T195-T207.